Korean J. Chem. Eng., 40(1), 46-56 (2023)
DOI: 10.1007/s11814-022-1252-7

pISSN: 0256-1115
eISSN: 1975-7220

Droplet size distribution in a biphasic liquid reactor for understanding the impact of various dual impeller designs on the morphology of S-PVC

Jeil Park, Wonhyeong Lee, and Jae W. Lee†

Department of Chemical and Biomolecular Engineering, KAIST, 291 Daehak-ro, Yuseong-gu, Daejeon 34141, Korea

(*Received 13 June 2022 • Revised 1 August 2022 • Accepted 10 August 2022*)

Abstract−This study investigated the effect of dual impeller geometry on the droplet size in the suspension-PVC (S-PVC) polymerization process. To simulate the process, 1,2-dichloroethane was used as a dispersed phase, because it has been used to replace the toxic vinyl chloride monomer (VCM). Using a borescope method, a droplet size was measured for a biphasic liquid system, and the Sauter mean diameter increased by 46.5% as the upper paddle impeller was replaced by 20° pitched paddle. It also increased when the impeller diameter and the blade width increased. Considering this effect, a geometrical factor (F) was revised, and a calculated maximum energy dissipation rate was used for establishing the Sauter mean diameter correlation. The proposed correlation can estimate the Sauter mean diameter within ±20% error, and one can predict the normality of the polymerization under specific impeller geometry using this correlation.

Keywords: Dual Impeller Geometry, S-PVC, Borescope, Maximum Energy Dissipation Rate, Sauter Mean Diameter

INTRODUCTION

Many efforts have been made to improve product yields through facilitated mass and heat transfer in vapor-solid [1,2] and liquid-liquid reactor units [3,4]. In particular, a stirred liquid-liquid reactor showed high product selectivity despite its simple vessel and impeller structure [5,6], as vapor-liquid reaction systems uses various forms of simple gas distributors [7,8]. Since reaction occurs at the interface between the dispersed phase droplet and the continuous phase, the efficiency of the process depends on the droplet size. Thus, controlling and predicting the droplet size under certain conditions would be a great help for the design and scale-up of the stirred liquid-liquid reactor.

One of the main industrial processes that uses stirred liquid-liquid reactor is the suspension-PVC (S-PVC) polymerization process [9,10]. In this process, the size of the final S-PVC resin can be estimated if the droplet size in the stirred liquid-liquid reactor is predictable. Droplets produced by the dispersion of vinyl chloride monomer (VCM) in the water are known to have little change in size after a certain conversion, due to the surrounding skin formed at the surface of the droplet as the reaction progresses [11,12]. Since the surrounding skin is formed at the relatively early stage of the reaction [12,13], the size of the initially produced droplet is bound to have a significant association with the final S-PVC resin size. In addition, the size of the VCM droplet is related to the abnormal S-PVC particle, fisheye. Fisheye is a rigid sphere particle that grows independently without breakup and reduces the processability since it does not absorb plasticizers. However, its occurrence may be reduced if a sufficient flow is applied to the entire liquid phase inside the reactor. Kobayashi et al. [14] added an auxiliary blade to the existing Brumagine type impeller for the reinforcement of the axial mixing and, as a result, the number of fisheye has been greatly reduced. Nevertheless, the modified impeller used in the literature is not a common form, which makes it difficult to apply to other reaction systems.

Thus, in this study, a widely used paddle impeller and pitched paddle impeller were adopted, and the droplet size was measured in a stirred liquid-liquid reactor. Unlike many previous studies using lab scale stirred reactor and a single impeller [15-18], a dual impeller system was used for the 100 liter scale reactor in this study since the single impeller is not suitable for large scale reactors [19,20]. Since it is known to have a high hydraulic efficiency when the pitched paddle impeller is located above and the paddle impeller is below [21], the geometry of the lower paddle impeller was fixed and only the upper pitched paddle was changed to investigate the effect of axial mixing on the droplet size. In addition, 1,2-dichloroethane (DCE) was used instead of toxic VCM, as it was used to simulate the S-PVC production process in the previous literature [22].

To measure the droplet size, many techniques have been used. When the droplet images are taken at the outside of the reactor [23,24], the reliability of the data cannot be ensured because only the droplets located at the wall of the reactor are photographed. Furthermore, the image of the droplets cannot be obtained if the liquid mixture inside the reactor becomes blurry. For the case of encapsulation and sampling [25-28], there is a possibility of coalescence between the droplets during the removal of the liquid sample. On the other hand, the borescope system can minimize the distortion of the droplet image, since it measures the droplet size directly at the inside of the liquid mixture in the reactor [15,16,29,30]. Since a large size reactor of 100 liters was used, the number of sampling locations was increased to three, taking a droplet image and calculat-

---

†To whom correspondence should be addressed.
E-mail: jaewlee@kaist.ac.kr

ing the Sauter mean diameter for each location.

In addition, this study proposes the Sauter mean diameter correlation to enable the prediction of the S-PVC resin size. Unlike most of the previous Sauter mean diameter correlations, which were established mainly by the property of the liquid phases [15,17,25, 31-34], we used a maximum energy dissipation rate (ε_{max}) since the energy dissipation takes place mainly in the vicinity of the impeller and it plays an important role in determining the droplet size. Furthermore, the effect of the impeller geometry on the Sauter mean diameter was reflected by using ε_{max} for the correlation. It is helpful to understand how the changes in dual impeller geometry affect the size and morphology of the S-PVC resin in the vinyl chloride polymerization process.

EXPERIMENTAL SECTION

1. Experimental Setup

A stainless steel reactor with a diameter of 40 cm and a height of 80 cm was used for the experiment. Inside the reactor, twelve cylindrical baffles with a diameter of 2 cm were placed 10 cm from the reactor center to reduce the vortex. To maintain the temperature of the reactor at 25 °C, a heating jacket was used, and the difference between the actual temperature and the set point was within ±1 °C. In addition, a borescope system was used for the droplet image acquisition, as shown in Fig. 1. To minimize the disturbance from the borescope, we used a borescope with a small diameter (94 cm length, 0.72 cm diameter; Gradient Lens Corporation, Hawkeye Pro Super Hardy, USA). The borescope was connected to a CCD camera (Sony, XCD-U100, Japan) and a xenon lamp (Excelitas Technologies, X-1500, USA) using a light guide. In addition, a personal computer with trigger software was also connected, so it was possible to shoot and save the droplet image. As illustrated in Fig. 2(a), the borescope was inserted into the reactor through the hole of the reactor upper plate. To prevent backflow, the borescope was covered with a stainless steel tube with a 1/2″ diameter, and a lens (12.5 mm diameter, 1.75 mm thickness; Edmund optics, BOROFLOAT® Borosilicate Windows, USA) was attached at the end of the tube. Since the volume of the reactor is large (ca. 100 liter) and a dual impeller is used, three sampling locations were employed and the droplet size was measured next to and between the two impellers.

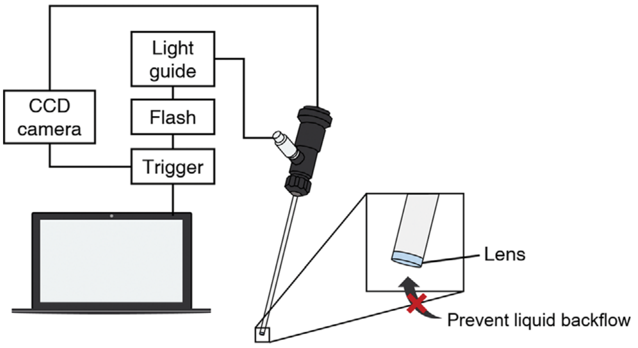

Fig. 1. Borescope system for the measurement of Sauter mean diameter.

For a paddle-paddle dual impeller system, a three-blade stainless steel paddle impeller (0.1115 m in diameter and 0.037 m blade in width; Fig. 2(b)) was used for both impellers. In the case of a pitched paddle-paddle dual impeller system, a three-blade stainless steel pitched paddle impeller (10/20° blade angle, 0.1115-0.1215 m diameter, and 0.037-0.057 m blade width; Fig. 2(c)) was used as an upper impeller while the aforementioned paddle impeller was used as a lower impeller. By using a pitched paddle with a small impeller blade angle, some extent of axial mixing occurred without making the droplet size too large, since the increase of impeller blade angle results in the increase of the Sauter mean diameter [35,36]. The detailed geometries of the impellers used in this study are presented in Table 1.

2. Borescope System Calibration

To calculate the actual size of the droplet obtained by the borescope system, an object that can be a reference is required. For the reference material, three glass bead sets with diameters of 2.0 mm (Glastechnique, Germany), 0.25 mm (SUPELCO, USA), and 0.075 mm (SUPELCO, USA) were used. Before the calibration, the focal

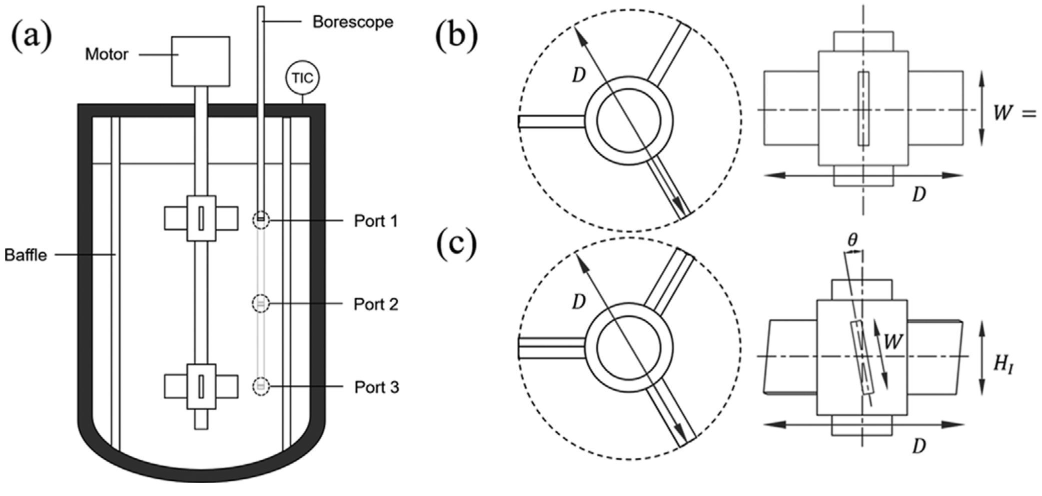

Fig. 2. Schematic diagram of the experimental apparatus: (a) stirred tank with the dual impeller and the borescope system (here, only paddle-paddle impeller system is presented); (b) paddle impeller; (c) pitched paddle impeller.

Table 1. Summary of the upper and lower impeller geometries used in this study

No.	θ_u (°)	D_u (m)	W_u (m)	θ_l (°)	D_l (m)	W_l (m)
1	0	0.1115	0.037	0	0.1115	0.037
2	10	0.1115	0.037	0	0.1115	0.037
3	20	0.1115	0.037	0	0.1115	0.037
4	10	0.1145	0.037	0	0.1115	0.037
5	10	0.1185	0.037	0	0.1115	0.037
6	10	0.1215	0.037	0	0.1115	0.037
7	10	0.1115	0.047	0	0.1115	0.037
8	10	0.1115	0.057	0	0.1115	0.037

Table 2. Density, surface tension, viscosity, and interfacial tension for the two liquid phases at 25 °C

Substance	Density (kg/m^3)	Surface tension (mN/m)	Viscosity (cP)	Interfacial tension (mN/m)
Water	997	71.976	0.890	28.43
DCE	1,245	31.860	0.779	

length of the CCD camera was adjusted so that the sharp borderline can be seen when the glass bead lying just in front of the lens is photographed. Over 200 glass bead images were taken to obtain reliable data, and the size of the glass bead represented by pixel was measured using the Adobe Photoshop program. Since the actual sizes of the glass beads are known, the actual size of one pixel was calculated. Three sizes obtained by each experiment were averaged and used as a reference size for the further droplet size measurement.

3. Sauter Mean Diameter Measurement

To measure the Sauter mean diameter, we used tap water and extra pure grade DCE (99.0%, SAMCHUN Pure Chemicals, Korea) for the aqueous phase and the organic phase, respectively. The properties of both phases are presented in Table 2. The density of the aqueous phase was obtained from Rumble et al. [37] and the surface tension of the aqueous phase was calculated by the equation of Vargaftik et al. [38]. For the viscosity of water, the value of Laliberté et al. [39] was used. The density, surface tension, and viscosity of the organic phase were obtained from Rumble et al. [37] and the interfacial tension between two phases was obtained from the Girault et al. [40].

The droplet size was measured at 25 °C and impeller speed of 300-600 rpm. Then, the fluid flow in the reactor was fully turbulent regime since the minimum Reynolds number was 7.9×10^4. Throughout the experiment, both an aqueous phase of 50 L and an organic phase of 30 L were used. Thus, the organic phase holdup (ϕ) was 0.375, which is relatively large compared to previous studies [24,27,31,32]. As listed in Table 1, only the upper impeller was switched according to its geometry change while the volumetric ratio of the two phases was fixed. After the two phases were carefully poured into the reactor, agitation was started with the impeller speed set. Considering that the size of the reactor we used was large, we doubled the previously reported stabilization time of 10 min [30] and investigated whether the 20 min of stabilization was sufficient. The details for the experiment and its result are described in the Supplementary Information (Fig. S1). To ensure the reliability of the data, 200 droplets were known to be sufficient to obtain the size distribution [29,30]. After obtaining over 200 droplet images, their sizes were measured using the Adobe Photoshop program. Using the actual size of one pixel obtained from the calibration of the borescope system, the droplet sizes were converted to actual sizes. With these data, the Sauter mean diameter (d_{32}) was calculated using Eq. (1), where n_i and d_i are the number of droplets and the diameter of the droplet, respectively. To ensure the reliability of the data, the whole experiment was repeated three times at each condition and the averaged value was used.

$$d_{32}=\frac{\Sigma_i n_i d_i^3}{\Sigma_i n_i d_i^2} \tag{1}$$

After calculating the Sauter mean diameter, the effects of blade angle, impeller diameter, and impeller width were analyzed using the design of experiments (DOE) software, Minitab 19. DOE has been widely used to evaluate the effectiveness of parameters [41-43], and we obtained a residual plot and a contour plot using three 2-factor general full factorial designs.

4. Sauter Mean Diameter Estimation

Many prior studies have proposed the Sauter mean diameter correlation, which includes the properties of the two liquid phases such as density, viscosity, and interfacial tension [17,32,44,45]. However, they did not properly reflect the impeller geometry and its effect, except the impeller diameter. Thus, we chose the correlation of Bliatsiou et al. [35] as a basic form, since their correlation reflected the effect of impeller geometry, as presented in Eq. (2). Here, C_1-C_3 are constants. In addition, ε_{max} can be calculated by using the mean energy dissipation rate $\bar{\varepsilon}$ and the geometrical factor F, suggested by Henzler and Biedermann [46] (Equation 3). In Eq. (3), the effect of impeller blade angle θ is reflected as a term $\cos\theta$.

$$d_{32}=C_1\varepsilon_{max}^{C_2} \text{ with } \varepsilon_{max}=C_3\frac{\bar{\varepsilon}}{F} \tag{2}$$

$$F=F'(\cos\theta)^{1.15} \text{ with } F'=\left(\frac{D}{T}\right)^2\left(\frac{H_I}{D}\right)^{2/3}N_B^{0.6}N_I^{2/3}\left(\frac{H}{T}\right)^{-2/3} \tag{3}$$

To obtain ε_{max}, $\bar{\varepsilon}$ was calculated from the sum of the power consumptions for each impeller obtained by the computational fluid dynamics (CFD) study. Detailed method of the CFD study is given in Section 2.5.

For ports 1 and 3, ε_{max} was used for the Sauter mean diameter fitting since ports 1 and 3 were most influenced by the upper and lower impeller, respectively. On the other hand, for port 2, $\bar{\varepsilon}$ was used because it was the least influenced region by the two impellers.

In addition, the circulation frequency ($1/t_c$) was used for the Sauter mean diameter fitting to reflect the effect of the flow circulation on the droplet size. First, the impeller flow number (Fl) was calculated using the power number and the equation of Jüsten et al. [47] which used the power number for the flow number estimation. Then, the circulation frequency for each impeller was calculated using the flow number and the equation of Smith et al. [48], which is $(1/t_c)=(Fl \cdot ND^3/V)$. For ports 1 and 3, the circulation frequency of nearby impeller (upper and lower impeller, respectively) was used for the Sauter mean diameter fitting, and for port 2 the two circulation frequencies were used together since the droplets at port 2 were affected by the flow created by both impellers. The Sauter mean diameter correlation was revised with multiple regressions, and the estimated Sauter mean diameter was compared with the experimental results.

5. CFD Study for the Impeller Power Number

A three-dimensional CFD technique using ANSYS FLUENT R1 was employed to calculate the impeller power number for the various dual impeller set which were used in this study (see Table 1). The hexa mesh was used for the 100 L reactor and the dual impeller system, and the mesh was densely generated at the interface and vortex generation position, as shown in Fig. 3.

For the numerical simulation, we used Eulerian for a multiphase model and realizable k-ε with scalable wall functions for the turbulence model. For the drag model, Schiller-Naumann model was used, and Troshko-Hassan model was used for the turbulence interaction. In addition, multiple reference frame (MRF) model was used for the dual impeller system, and a stationary reference frame was used for the stationary region.

To verify the reliability of the simulation results, a grid independence test was conducted. The effect of four grid numbers (ranged from 111,546 to 404,164) on the total torque of the paddle-paddle dual impeller system was investigated.

In addition, to confirm how similar the CFD results are to the actual flow phenomenon, the depth of the vortex and the increase of the liquid surface height during the agitation were measured and compared with the CFD results. For a water-DCE mixture, as the liquid phase became blurred during the agitation, it was difficult to measure the vortex depth from the outside of the reactor. Thus, 80 L of water was used instead of water-DCE mixture and stirred at 600 rpm. The experiment was conducted at the base impeller position and the upper impeller was moved 40 mm upward. First, after the stabilization time of 20 min, a video was taken for 30 sec (in real time) using a high-speed camera with 6 fps; thus the length of the video was 3 min. Afterwards, an image was captured every 1 sec (based on the time scale of the video) as presented in Fig. 4, and a total of 100 snapshots were obtained. For each picture, the vortex depth and the difference in water surface height before and after the agitation were measured. Thereafter, the average values of these and the CFD results were compared.

Afterwards, using the torque (M) obtained by the CFD simulation, the power consumption (P) and power number (Ne) of the upper/lower impellers for each dual impeller set were calculated, as shown in Eqs. (4) and (5).

$$Ne=\frac{P}{\rho N^3 D^5} \tag{4}$$

$$P=2\pi MN \tag{5}$$

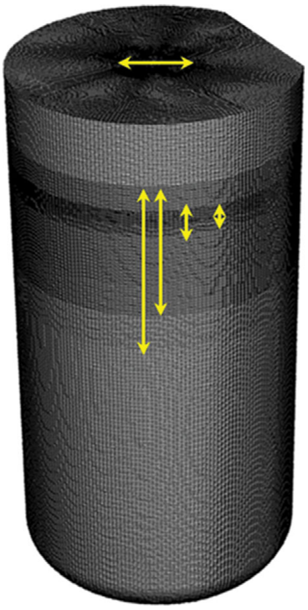

Fig. 3. Mesh generated by ANSYS FLUENT for the 100 L reactor with a dual impeller.

Fig. 4. Vortex and surface height image taken using the high-speed camera for base impeller position.

The power numbers at the impeller speed of 300 rpm were used for other impeller speeds, since the power number is known to change only slightly when the Reynolds number is large enough ($>10^3$) and the lowest Reynolds number in our system was 7.9×10^4.

RESULTS AND DISCUSSION

1. Calibration of the Borescope System

The borescope was calibrated by taking the photo of the glass bead sets with diameters of 2, 0.25, and 0.075 mm. As illustrated in Figs. 5(a)-(c), the image of the glass beads was successfully obtained, and the small characteristic circular pattern is shown in each glass bead image. These circles were created by the reflection of the flashlight [29] and used as a standard point for the measurement of the droplet radius.

Using the Adobe Photoshop program, the sizes of the glass beads represented by pixels were measured and averaged. Since the size of the glass bead sets was known, the actual size of one pixel was calculated by the proportional relation. The high reproducibility was confirmed because the three pixel sizes were quite similar (2.87 μm/pixel for a 2 mm glass bead, 2.69 μm/pixel for a 0.25 mm glass bead, and 2.72 μm/pixel for a 0.075 mm glass bead), and each averaged value of these three was used for the droplet size measurements.

2. Verification of the Borescope System

To calculate the Sauter mean diameter, the photos of the DCE droplets were taken at various impeller speeds and types. As shown in Fig. 6(a), the water-DCE mixture became opaque with the rising impeller speed. However, by using a light source and high shutter speed, the image of the droplet was successfully obtained at a high impeller speed of 600 rpm. Thus, it is a huge advantage of the borescope system that the image of the droplet can be obtained under the invisible condition of bare human sight. The actual image obtained from port 1 of the paddle-paddle dual impeller is illustrated in Figs. 6(b)-(e).

3. Droplet Size Distribution

The droplet size distribution was calculated using all droplet sizes obtained through three experiments, and the results are shown in Figs. 7-9. In Fig. 7, the effect of the impeller blade angle on the droplet size distribution is presented. For all three impellers, the droplet size distribution became narrower as the impeller speed rose. These results were consistent with the experimental data of the previous study [12]. Notably, for the paddle-paddle impeller, there was no major change in the size distribution at an impeller speed higher than 300 rpm. This indicates that when a paddle impeller having good breakup performance is used, the decrease of the droplet size may not be large even with the impeller speed in-

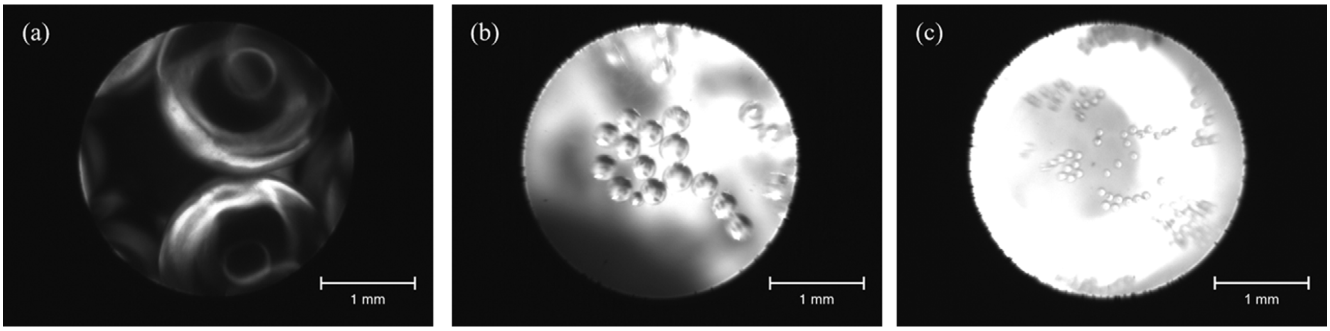

Fig. 5. Glass bead photos taken by the borescope system; (a) 2 mm glass beads; (b) 0.25 mm glass beads; (c) 0.075 mm glass beads.

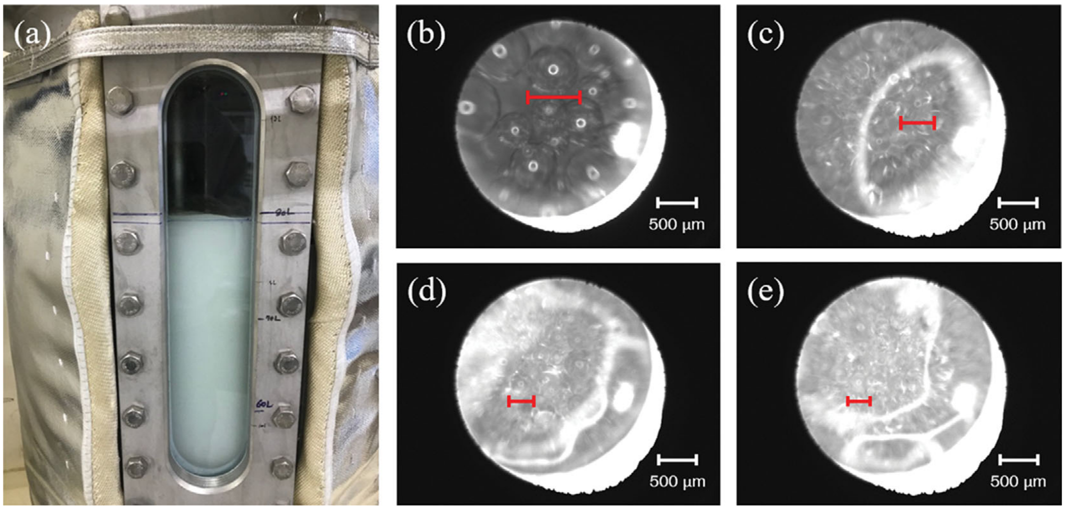

Fig. 6. Blurry water-DCE mixture and the actual droplet photos at port 1 of the paddle-paddle dual impeller: (a) 400 rpm; (b) 300 rpm; (c) 400 rpm; (d) 500 rpm; (e) 600 rpm.

creased. Thus, under the paddle-paddle impeller, the droplet size is already sufficiently diminished from the impeller speed of 400 rpm. This phenomenon was also found in the previous study [49]: the droplet size distribution became much narrower when the impeller speed increased from 350 to 450 rpm. However, when the impeller speed further increased to 550 rpm, the droplet size distribution was almost the same as that at 450 rpm. In addition, since the organic phase holdup they used was 0.4 [50], it is quite similar to the organic phase holdup used in this study (0.375).

Compared to the paddle-paddle impeller, another type of pitched paddle-paddle impeller showed relatively distinguished droplet size distribution in Figs. 7(b) and 7(c). In particular, at the 20° pitched paddle-paddle impeller, the droplet size distribution was relatively broad even at a high impeller speed of 600 rpm.

Fig. 8 depicts the influence of the upper impeller diameter on the droplet size distribution for the pitched paddle-paddle impeller

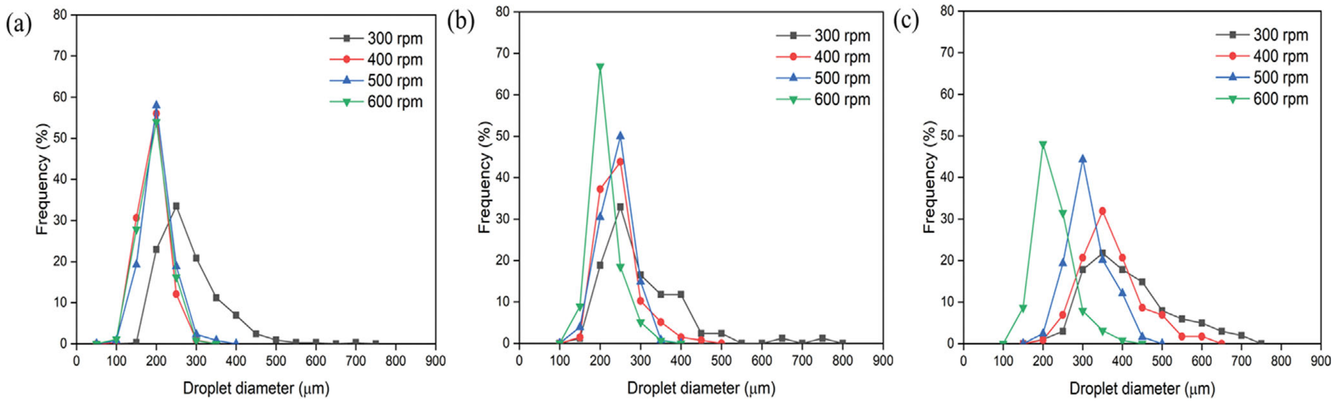

Fig. 7. Droplet size distribution at port 1, 111.5 mm diameter: (a) paddle-paddle impeller; (b) 10° pitched paddle-paddle impeller; (c) 20° pitched paddle-paddle impeller.

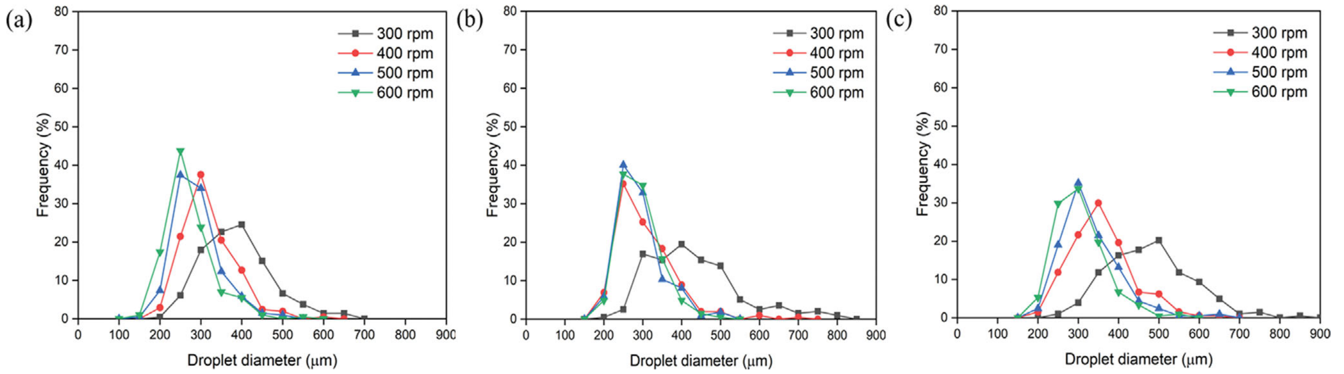

Fig. 8. Droplet size distribution at 10° pitched paddle-paddle impeller, port 1: (a) 114.5 mm diameter; (b) 118.5 mm diameter; (c) 121.5 mm diameter.

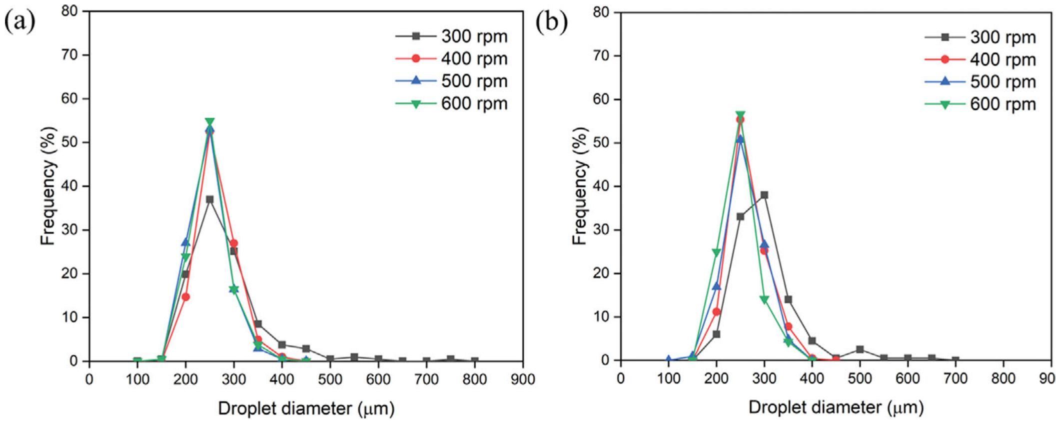

Fig. 9. Droplet size distribution at 10° pitched paddle-paddle impeller, port 1: (a) 47 mm impeller blade width; (b) 57 mm impeller blade width.

with 10° blade angle. It is expected that the droplet size will decrease when the impeller diameter becomes large, because a larger impeller diameter results in higher impeller power, which can make the droplet breakup process dominant. However, the droplet size distribution at this condition moved to the right (larger) as the impeller diameter increased. Fig. 9 illustrates the change of the droplet size distribution when the blade width of the 10° pitched paddle impeller increased. Unlike the impeller blade angle and diameter, the effect of the impeller blade width on the droplet size distribution seemed less pronounced. The droplet size distribution was approximately the same for all impeller speeds except 300 rpm.

4. Sauter Mean Diameter Calculation

The effect of the blade angle of the upper impeller on the Sauter mean diameter is illustrated in Fig. 10. For all sampling locations, the Sauter mean diameter greatly increases as the impeller blade angle increases. When the same impeller diameter is used, the pitched paddle impeller shows smaller power than the paddle impeller. In addition, when the paddle impeller is changed to the pitched paddle impeller, axial velocity increases: thus, the droplets at the vicinity of the impeller are pushed away from the impeller zone and the breakage of droplets becomes lowered. The Sauter mean diameter will increase since the impeller zone plays an important role in the droplet breakup. Thus, the incremental trend of the Sauter mean diameter with the rise of the impeller blade angle is predictable. At the same impeller diameter of 111.5 mm, the Sauter mean diameter greatly increased (compared to the paddle impeller case, 17.3% increase for the 10° pitched paddle impeller, and 46.5% increase for the 20° pitched paddle impeller) while the impeller blade angle changed slightly.

In Fig. 11, the Sauter mean diameter at different upper pitched paddle diameters is presented. As the diameter of the 10° pitched paddle impeller increased, the Sauter mean diameter at port 2 and 3 became larger, despite the increase in the impeller power consumption. When the impeller diameter of the pitched paddle increased, not only the impeller power was changed, but also the axial flow was enhanced. The paddle impeller clearly has a certain level of axial flow, since the flow produced from the impeller with zero blade angle (paddle impeller) can be directed upward and downward [51]. However, when a pitched paddle was used, the axial flow was intensified considerably. To confirm this, CFD simulations were conducted, as described in the Supplementary Information (Fig. S2). Although the impeller blade angle increased by only 10 degrees, the axial velocity increased significantly, while the radial velocity greatly decreased (Fig. S2(b)). Thus, the axial mixing increased substantially due to the increased impeller blade angle, and the breakup efficiency decreased as the radial velocity reduced.

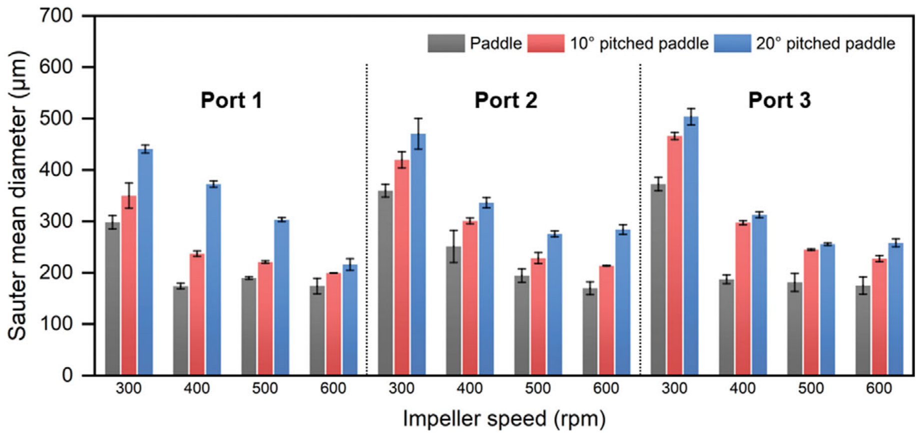

Fig. 10. Measured Sauter mean diameter with impeller speed and upper impeller blade angle.

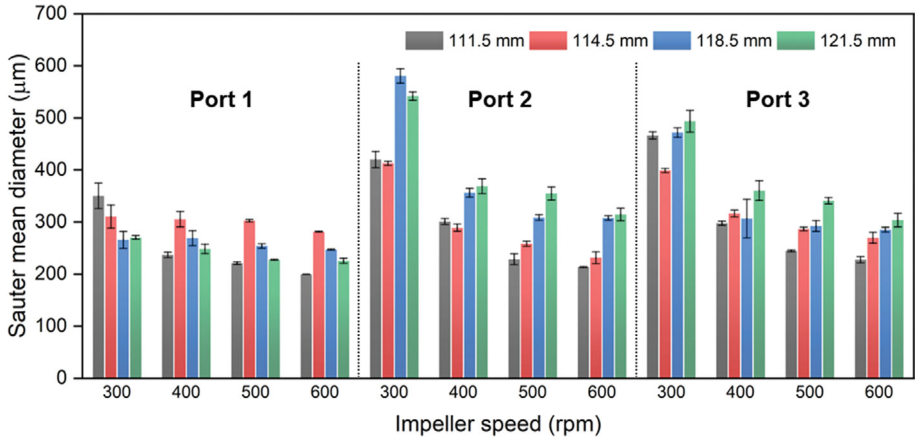

Fig. 11. Measured Sauter mean diameter with different impeller speed and upper 10° pitched paddle impeller diameter.

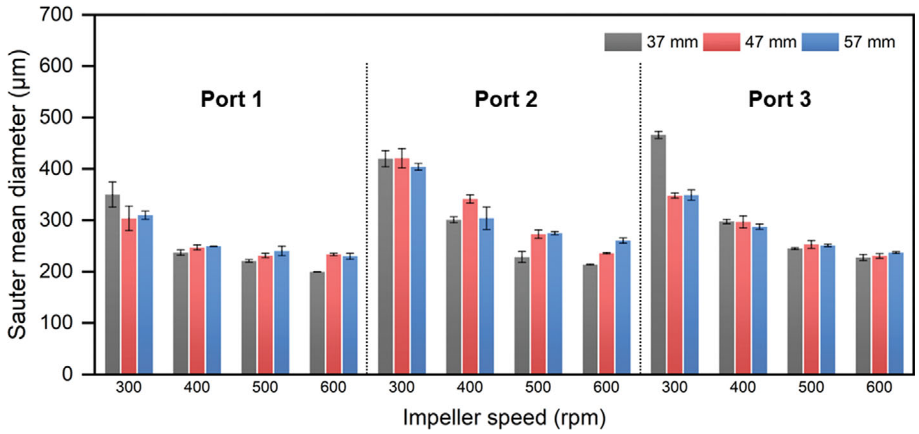

Fig. 12. Measured Sauter mean diameter with different impeller speed and upper 10° pitched paddle impeller blade width.

The effect of increased axial mixing on the rising droplet size can also be found in the previous study [12]. They reported the reinforced axial mixing by adding a small blade to the existing impeller blade. Thus, the impeller power consumption also increased. However, the droplet size measurement shows that the number of 60-100 mesh particles decreased, while the number of 145-200 mesh particles increased compared to the normal impeller. As a result, the size increased despite the increased impeller power consumption. It is conjectured that the Sauter mean diameter increased because the increased impeller power consumption has a greater effect on the enhancement in axial flow rather than the increase in breakup.

On the other hand, the Sauter mean diameter at port 1 showed different trend than the other two. It was confirmed that the increase in axial flow initially increases the droplet size, but eventually the breakup effect becomes much greater if the impeller diameter continuously increases. Since most breakup processes occur in the impeller zone around the impeller [52-54], the effect of the increased impeller diameter may have been greatest at port 1, which was located closest to the changed pitched paddle.

Fig. 12 shows the effect of the blade width of the upper 10° pitched paddle impeller on the Sauter mean diameter. The flow change caused by the decreased distance between the impeller tip and the tank wall can be excluded because the impeller diameter is fixed at 111.5 mm. Therefore, the effect of the increased axial flow can be clearly investigated. The Sauter mean diameter increased as the impeller blade width increased, and this phenomenon was more pronounced at higher impeller speed. Like the increase in the pitched paddle diameter, the decrease in the droplet residence time in the impeller zone due to the increase in axial velocity would have a greater effect on the Sauter mean diameter than the increase in power consumption due to the increase in the impeller width (droplet breakup).

However, the effect of increasing the impeller blade width on the Sauter mean diameter was less than that of increasing the impeller diameter (Fig. 11). It appears that the impeller power is more affected by the impeller diameter than by the impeller width. Hudcova et al. [51] showed that even if the impeller blade width is doubled, the impeller power consumption only increases by 30%. Thus, when the impeller power consumption should increase to intensify the axial flow, it is more effective to increase the impeller diameter than the impeller blade width. Based on the calculated Sauter mean diameter values, the effect of three impeller geometries and the impeller speed was analyzed using a DOE software Minitab 19. The residual plots and contour plots for the impeller speed and each impeller geometry are shown in Supplementary Information (Fig. S3-S5).

In summary, slightly increasing the impeller blade angle increased the axial flow significantly. On the other hand, the radial velocity substantially reduced, resulting in the considerable increase in the Sauter mean diameter. Thus, using a pitched paddle impeller with a large blade angle to reduce the number of fisheye in the S-PVC production process may result in insufficient breakup, and large particles such as fisheye can be made. In addition, in the case of pitched paddle, the Sauter mean diameter tended to increase even if the impeller power consumption increased by changing the impeller diameter or blade width. However, since the continuous increase in the impeller diameter of the pitched paddle eventually reduced the Sauter mean diameter (at port 1), the pitched paddle impeller with a large diameter and small blade angle is expected to help reduce fisheye by producing small size droplets and narrow droplet size distributions.

5. Calculation of the Impeller Power Number by CFD Study

The results of the grid independence tests are described in Table 3. The difference between the last two results was insignificant (<1%). Thus, a grid number of 232,836 was chosen for the simulation.

Fig. 13 shows vortex and liquid phase surfaces generated at different upper impeller positions, determined by the CFD simulations. It can be confirmed that as the impeller is positioned above, the vortex deepens and the liquid phase surface increases. Between these simulation and actual experimental results, there was no significant difference as shown in Table 4. Thus, using torque results

Table 3. Total torque of the paddle-paddle dual impeller at 600 rpm with different grid numbers

Number of grids	115,546	159,510	232,836	404,164
Total torque (N·m)	2.020	1.980	1.952	1.933

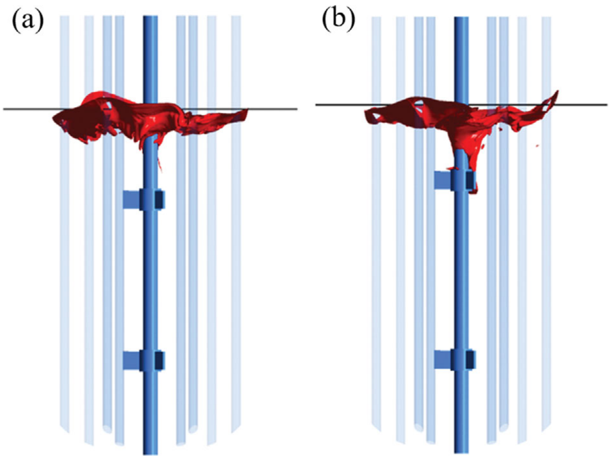

Fig. 13. Vortex and liquid phase surface generated at different upper impeller positions in CFD simulations of (a) base position; (b) 40 mm up.

obtained through the CFD study, the power consumption and power number of all impeller sets were calculated and the results are listed in Table 5.

6. Sauter Mean Diameter Estimation

According to Eqs. (2) and (3), d_{32} should decrease due to the increased impeller blade angle, since F decreases with the increasing upper impeller blade angle (θ_u) and Bliatsiou et al. [35] used negative b value. This is in contrast to experimental results, since the larger impeller blade angle results in the weaker droplet breakup at the same impeller diameter. Thus, we revised Eqs. (2) and (3) into Eq. (6). In this equation, the effect of the axial mixing is reflected by using the term of $\sin 2\theta_u$, since the axial mixing increases as θ_u increases and reaches the maximum when the blade angle is equal to 45°. Here, a, b, and c are constants.

$$\varepsilon_{max} = \mathrm{a}\left(\frac{\bar{\varepsilon}}{\mathrm{F}}\right) \text{ with } \mathrm{F} = \mathrm{F}'(\mathrm{b} + \sin 2\theta_u)^c \tag{6}$$

In Eq. (7) and Table 6, the proposed Sauter mean diameter correlations for each sampling location and each constant obtained by multiple regression are presented, respectively. The Sauter mean diameter estimated by the proposed correlation can predict the experimental results within ±20% error, as shown in Fig. 14. It can successfully reflect the effect of the impeller type and power, despite that the substantial change in the droplet size when they varied.

$$\begin{aligned} &\text{Port 1: } \mathrm{d}_{32} = \mathrm{C}_1 \varepsilon_{max}{}^{C_2}\left(\frac{1}{\mathrm{t}_{c\_u}}\right)^{C_3} \\ &\text{Port 2: } \mathrm{d}_{32} = \mathrm{C}_1 \bar{\varepsilon}^{C_2}\left(\frac{1}{\mathrm{t}_{c\_u}}\right)^{C_3}\left(\frac{1}{\mathrm{t}_{c\_l}}\right)^{C_4} \\ &\text{Port 3: } \mathrm{d}_{32} = \mathrm{C}_1 \varepsilon_{max}{}^{C_2}\left(\frac{1}{\mathrm{t}_{c\_l}}\right)^{C_3} \end{aligned} \tag{7}$$

Table 4. Comparison between the experimentally measured surface level increase/average vortex depth and the CFD results at different impeller position

	Surface level increase (base position)	Average vortex depth (base position)	Surface level increase (40 mm up)	Average vortex depth (40 mm up)
Experiment (mm)	40	48	50	130
CFD (mm)	42	49	52	128

Table 5. Impeller power consumption and power number at 600 rpm for the various types of impeller used in this study, calculated by the CFD study

No.	θ_u (°)	D_u (m)	W_u (m)	P_u (W)	P_l (W)	Ne_u	Ne_l
1	0	0.1115	0.037	63.56	64.13	3.35	3.38
2	10	0.1115	0.037	55.21	63.75	2.91	3.36
3	20	0.1115	0.037	46.67	65.64	2.46	3.46
4	10	0.1145	0.037	55.68	63.94	2.57	3.37
5	10	0.1185	0.037	63.54	64.69	2.47	3.41
6	10	0.1215	0.037	70.83	66.02	2.43	3.48
7	10	0.1115	0.047	66.21	63.18	3.49	3.33
8	10	0.1115	0.057	76.46	61.09	4.03	3.22

*Here, only upper impeller geometry was presented since the lower impeller remained unchanged.

Table 6. Multiple regression results of each constant for different sampling locations

Port	a	b	c	C_1	C_2	C_3	C_4
1	0.140	0.667	8.37	224	−0.069	−0.199	-
2	-	-	-	266	−0.281	0.013	0.011
3	0.126	1.34	4.18	230	−0.059	−0.190	-

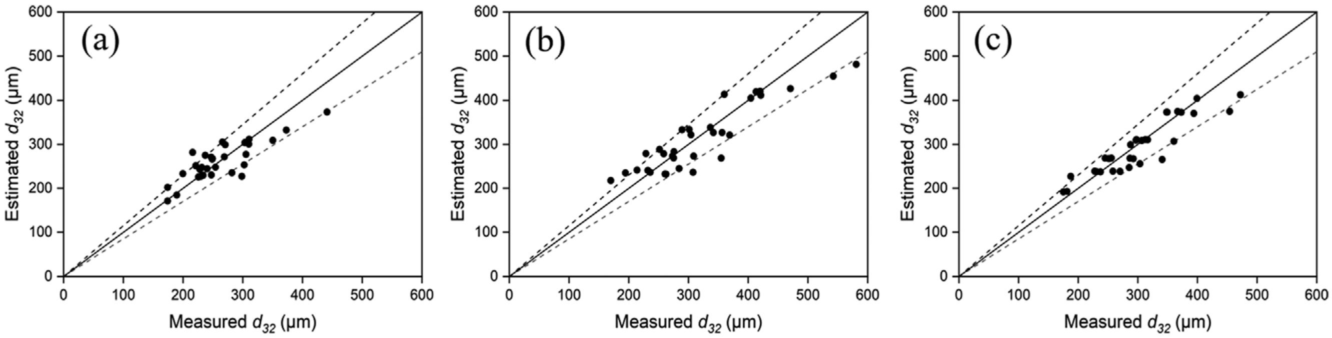

Fig. 14. Parity plots of Sauter mean diameter estimated by the correlation developed in this work: (a) port 1; (b) port 2; (c) port 3; the dash lines represent ±20% error.

CONCLUSIONS

This study investigated how the geometry of dual impellers, such as diameter, blade angle, and blade width in the S-PVC production process, affects the size of the organic phase droplet. A reactor of 100 L was used to reflect the characteristics of a commercial reactor. The Sauter mean diameter was greatly enlarged by 46.5% as the blade angle of the upper paddle increased by 20°. The Sauter mean diameter also increased by 54.8% and 15.4%, when the impeller diameter and width of the 10° pitched paddle was increased by 9.0% and 54.1%, respectively. Based on these results, it was found that both large impeller diameter and small blade angle are suitable for better processability of S-PVC resin. Furthermore, by suggesting the Sauter mean diameter correlation which reflects the effect of impeller geometry, it is possible to predict in advance whether abnormal polymerization will occur during S-PVC polymerization.

ACKNOWLEDGEMENT

This work was supported by the ERC Center funded by the National Research Foundation of Korea (NRF-2022R1A5A1033719).

NOMENCLATURE

Symbols Used

C_i : constants (i=1-4)
D : tank diameter [m]
D_I : impeller diameter [m]
d_i : droplet diameter [m]
d_{32} : Sauter mean diameter [m]
F : geometrical factor [-]
H : filling height of the stirred tank reactor [m]
H_I : vertical impeller height [m]
M : torque of the impeller [N m]
N : impeller speed [s^{-1}]
N_B : number of impeller blades [-]
N_I : number of impellers [-]
n_i : number of droplets
P : power consumption [W]
t : time [s]
$\frac{1}{t_c}$: circulation frequency [s^{-1}]
$\frac{1}{t_{c\_l}}$: circulation frequency of lower impeller [s^{-1}]
$\frac{1}{t_{c\_u}}$: circulation frequency of upper impeller [s^{-1}]
V : filling volume of the stirred tank reactor [m^3]
W : impeller blade width [m]

Greek Symbols

$\bar{\varepsilon}$: mean specific energy dissipation rate [W kg^{-1}]
ε_{max} : maximum energy dissipation rate [W kg^{-1}]
θ : impeller blade angle of the upper impeller [°]
ρ : density [kg m^{-3}]
σ : surface tension [mN m^{-1}]

Subscripts

l : lower impeller
u : upper impeller

Dimensionless Number

Fl : impeller flow number
Ne : impeller power number
We_I : impeller Weber number, $\frac{N^2D^3\rho}{\sigma}$

SUPPORTING INFORMATION

Additional information as noted in the text. This information is available via the Internet at http://www.springer.com/chemistry/journal/11814.

REFERENCES

1. J. R. Lee, N. Hasolli, K. S. Lee, K. Y. Lee and Y. O. Park, *Korean J. Chem. Eng.*, **36**, 1548 (2019).
2. J. W. Lee, Y. C. Ko, Y. K. Jung, K. S. Lee and E. S. Yoon, *Comput. Chem. Eng.*, **21**, S1105 (1997).
3. S. Samdavid, T. Renganathan and K. Krishnaiah, *Korean J. Chem. Eng.*, **39**, 86 (2022).
4. K. Rave, M. Hermes, D. Wirz, M. Hundshagen, A. Friebel, E. von Harbou, H. J. Bart and R. Skoda, *Chem. Eng. Sci.*, **253**, 117518 (2022).
5. D. E. Bergbreiter and S. D. Sung, *Adv. Synth. Catal.*, **348**, 1352 (2006).
6. B. Liu, N. Sun, Z. Jin, Y. Zhang and B. Sunden, *Ind. Eng. Chem.*

Res., **58**, 22376 (2019).

7. H. Im, J. Park and J. W. Lee, *ACS Omega*, **4**, 1329 (2019).
8. H. Im, S. Lee and J. W. Lee, *Chem. Eng. Res. Des.*, **136**, 654 (2018).
9. R. H. Burgess, *Manufacture and processing of PVC*, CRC Press (1981).
10. R. Darvishi, M. Nasr Esfahany and R. Bagheri, *J. Vinyl Addit. Technol.*, **22**, 470 (2016).
11. P. V. Smallwood, *Polymer (Guildf)*, **27**, 1609 (1986).
12. R. Guo, E. Yu, J. Liu and Z. Wei, *RSC Adv.*, **7**, 24022 (2017).
13. M. Zerfa and B. W. Brooks, *J. Appl. Polym. Sci.*, **60**, 2077 (1996).
14. T. Kobayashi, Y. Tomishima, T. Yamamoto and Y. Nojima, US Patent, 4,849,482 (1989).
15. J. Park, S. Lee and J. W. Lee, *Ind. Eng. Chem. Res.*, **57**, 2310 (2018).
16. A. Gäbler, M. Wegener, A. R. Paschedag and M. Kraume, *Chem. Eng. Sci.*, **61**, 3018 (2006).
17. C. Desnoyer, O. Masbernat and C. Gourdon, *Chem. Eng. Sci.*, **58**, 1353 (2003).
18. S. Choi, I. Jung, H. Kim, J. Na and J. M. Lee, *Korean J. Chem. Eng.*, **39**, 515 (2022).
19. N. Hardy, F. Augier, A. W. Nienow, C. Béal and F. Ben Chaabane, *Chem. Eng. Sci.*, **172**, 158 (2017).
20. D. Gu, Z. Liu, C. Xu, J. Li, C. Tao and Y. Wang, *Chem. Eng. Process. Process Intensif.*, **118**, 37 (2017).
21. V. Mishra and J. Joshi, *Chem. Eng. Res. Des.*, **72**, 657 (1994).
22. R. P. Borwankar, S. I. Chung and D. T. Wasan, *J. Appl. Polym. Sci.*, **32**, 5749 (1986).
23. A. W. Pacek, S. Chamsart, A. W. Nienow and A. Bakker, *Chem. Eng. Sci.*, **54**, 4211 (1999).
24. R. V. Calabrese, T. P. K. Chang and P. T. Dang, *AIChE J.*, **32**, 657 (1986).
25. Y. Mlynek and W. Resnick, *AIChE J.*, **18**, 122 (1972).
26. M. Laso, L. Steiner and S. Hartland, *Chem. Eng. Sci.*, **42**, 2437 (1987).
27. M. C. Ruiz, P. Lermanda and R. Padilla, *Hydrometallurgy*, **63**, 65 (2002).
28. S. Carrillo De Hert and T. L. Rodgers, *AIChE J.*, **64**, 3293 (2018).
29. J. Ritter and M. Kraume, *Chem. Eng. Technol.*, **23**, 579 (2000).
30. S. Lee and A. Varma, *AIChE J.*, **61**, 2228 (2015).
31. D. E. Brown and K. Pitt, *Chem. Eng. Sci.*, **29**, 345 (1974).
32. P. A. Quadros and C. M. S. G. Baptista, *Chem. Eng. Sci.*, **58**, 3935 (2003).
33. H. Im, J. Park and J. W. Lee, *Korean J. Chem. Eng.*, **36**, 1680 (2019).
34. R. Afshar Ghotli, M. R. Abbasi, A. H. Bagheri, A. A. A. Raman, S. Ibrahim and H. Bostanci, *J. Taiwan Inst. Chem. Eng.*, **100**, 26 (2019).
35. C. Bliatsiou, A. Malik, L. Böhm and M. Kraume, *Ind. Eng. Chem. Res.*, **58**, 2537 (2019).
36. J. Park, W. Ahan and J. W. Lee, *Korean J. Chem. Eng.*, **38**, 1348 (2021).
37. J. R. Rumble, D. R. Lide and T. J. Bruno, *CRC handbook of chemistry and physics*, CRC Press, Florida (2017).
38. N. B. Vargaftik, B. N. Volkov and L. D. Voljak, *J. Phys. Chem. Ref. Data*, **12**, 817 (1983).
39. M. Laliberté, *J. Chem. Eng. Data*, **52**, 321 (2007).
40. H. H. J. Girault, D. J. Schiffrin and B. D. V. Smith, *J. Colloid Interface Sci.*, **101**, 257 (1984).
41. V. Zeynali, J. Sargolzaei and A. H. Moghaddam, *Desalin. Water Treat.*, **56**, 24240 (2016).
42. J. Sargolzaei, A. H. Moghaddam and J. Shayegan, *Korean J. Chem. Eng.*, **28**, 1889 (2011).
43. S. M. A. Masoudi, A. Hedayati Moghaddam, J. Sargolzaei, A. Darroudi and V. Zeynali, *Environ. Prog. Sustain. Energy*, **37**, 1638 (2018).
44. C. A. Coulaloglou and L. L. Tavlarides, *AIChE J.*, **22**, 289 (1976).
45. E. G. Chatzi, C. J. Boutris and C. Kiparissides, *Ind. Eng. Chem. Res.*, **30**, 1307 (1991).
46. H.-J. Henzler and A. Biedermann, *Chemie Ing. Tech. - CIT*, **68**, 1546 (1996).
47. P. Jüsten, G. C. Paul, A. W. Nienow and C. R. Thomas, *Biotechnol. Bioeng.*, **52**, 672 (1996).
48. J. J. Smith, M. D. Lilly and R. I. Fox, *Biotechnol. Bioeng.*, **35**, 1011 (1990).
49. E. L. Paul, V. A. Atiemo-Obeng and S. M. Kresta, *Handbook of industrial mixing: Science and practice*, John Wiley & Sons (2003).
50. J. Lovick, A. A. Mouza, S. V. Paras, G. J. Lye and P. Angeli, *J. Chem. Technol. Biotechnol.*, **80**, 545 (2005).
51. V. Hudcova, V. Machon and A. W. Nienow, *Biotechnol. Bioeng.*, **34**, 617 (1989).
52. L. A. Cutter, *AIChE J.*, **12**, 35 (1966).
53. H. Wu and G. K. Patterson, *Chem. Eng. Sci.*, **44**, 2207 (1989).
54. J. Sheng, H. Meng and R. O. Fox, *Chem. Eng. Sci.*, **55**, 4423 (2000).